Phase control for quasi-2D blue emitters by spacer cation engineering†

Ho Won Tam,[a] Tik Lun Leung,[a] Wenting Sun,[a] Fangzhou Liu,[a] Chao Ma,[b] Kam Sing Wong,[b] Ivor Lončarić,[c] Luca Grisanti,[c] Juraj Ovčar,[c] Željko Skoko,[d] Jasminka Popović*[e] and Aleksandra B. Djurišić*[a]

The effect of alkylammonium tail length in phenyl-alkyl spacer cations in quasi-2D Ruddlesden–Popper perovskites on the phase distribution in low n films (n = 2 stoichiometry) is investigated. An increase in alkyl chain length suppresses the formation of the n = 1 phase (and consequently higher n phases), which is attributed to the change in the packing arrangement of spacer cations from parallel (one and two carbon atom alkyl chains) to non-parallel (3 carbon atom alkyl chains). A single blue emission peak corresponding to the n = 3 phase (466 nm) and n = 2 phase (436 nm) is obtained in the PL spectra of phenylpropylammonium quasi-2D perovskites with methylammonium (MA) and formamidinium (FA) cations, respectively. The same trends in phase distribution, namely a reduction in the proportion of the n = 1 phase with increasing alkyl chain length, are observed for both MA- and FA-based perovskites. However, FA-based samples exhibited higher crystallinity but worsened morphology (more pinholes) and less efficient funneling compared to MA-based samples. Consequently, efficient sky-blue LEDs with the highest EQE of 3.35% are obtained for $PPA_2MAPb_2Br_7$ perovskite.

Introduction

Metal halide perovskites are of significant interest for light emitting applications due to their high colour purity and consequently wide colour gamut, potential for high luminescence quantum yields, high carrier mobilities, and low temperature, low cost deposition.[1] Perovskite LEDs (PeLEDs) have demonstrated rapid progress since their first reports in 2014 with efficiencies of the order 10^{-2}% to over 20% at present for green, red, and near infrared PeLEDs.[1,2] However, the efficiency of blue LEDs is lagging behind those achieved in other spectral regions.[2,3] Therefore, there is considerable interest in the development of novel perovskite blue emitters.[3]

Among different kinds of perovskite emitters, quasi-2D layered perovskites are of particular interest due to their larger exciton binding energies and improved stability compared to the commonly used 3D perovskite materials.[1,4,5] Consequently, these materials have been extensively studied.[1–35] The Ruddlesden–Popper (RP) quasi-2D perovskites have a formula of $A_2'A_{n-1}B_nX_{3n+1}$, where A′ is the bulky spacer cation, A is a small organic cation or Cs^+, B is a divalent metal cation (commonly Pb^{2+} or Sn^{2+}), and X is a halide anion, while n is the number of layers of BX_6 octahedra separated by a bilayer of A′ spacer cations.[1,3] As n decreases, exciton binding energy and bandgap increase, while for $n = \infty$, the 3D perovskite ABX_3 is obtained.[1,3] Therefore, the emission properties can be modified by adjusting n, which is of significant interest to avoid issues related to halide de-mixing during operation, which leads to spectral instabilities in LEDs using mixed halide perovskite emitters.[2,23]

However, while the concept of band gap tuning *via* the selection of n works perfectly in the case of exfoliated single crystals, in the case of thin films, it is not so straightforward, since thin films of RP perovskites typically contain multiple n phases.[4,5,8,15,19,26] Due to the presence of multiple phases and the funneling phenomenon,[13,15,18,22,26] the films typically exhibit emission from the lowest band gap phase present, *i.e.* the largest n. As a result, even films that mainly consist of low n numbers (n = 2 or n = 3) tend to exhibit green emission centered at wavelengths over 500 nm instead of blue emission.[6,13,22,26] Hence, the achievement of blue emission can require the use of mixed halide anions,[22] which defeats the purpose of emission tuning by adjusting the number of layers n to avoid spectral instabilities related to ion migration induced halide segregation.[24] In addition, increased phase purity is desirable to improve

[a] Department of Physics, The University of Hong Kong, Pokfulam, Hong Kong. E-mail: dalek@hku.hk
[b] Department of Physics, The Hong Kong University of Science and Technology, Clearwater Bay, Hong Kong
[c] Division of Theoretical Physics, Ruđer Bošković Institute, Zagreb, Croatia
[d] Department of Physics, Faculty of Science, University of Zagreb, Croatia
[e] Division of Materials Physics, Ruđer Bošković Institute, Zagreb, Croatia. E-mail: Jasminka.Popovic@irb.hr

† Electronic supplementary information (ESI) available. See DOI: 10.1039/d0tc01631d

spectral stability.[29] Consequently, full control over the phase composition of the films is essential for the achievement of emission in the desired wavelength range.[5–8,14,19–21] Despite all attempts to achieve phase purity for some commonly used spacer cations, such as phenylethylammonium (PEA), it is well established that along with the formation of the desired n = 2 phase, crystallization of n = 1 phase often cannot be avoided.[8,19,21] For the PEA-based films prepared from stoichiometric n = 2 solutions, formation of the n = 1 phase also implies the unavoidable formation of higher n phases, which commonly results in efficient energy transfer to higher n phases[19,21] and green emission instead of the desired blue or sky-blue emission.

To achieve high n = 2 phase purity that would ensure blue emission, the choice of precursors, the excess amount of ligand, additives (molecules or nanoparticles), and the utilization of mixed small cations or mixed spacer cations have been investigated,[2,3,7,8,16,19,21,23] and improvements in the achieved emission spectra have been demonstrated. Among the mentioned approaches aiming to achieve high phase purity for low n numbers, one additional pathway, namely, the diversity of spacer cation structural features, represents a good alternative. Unfortunately, the relationship between the structure of spacer cations and the resulting film properties is still poorly understood, and moreover systematic investigations on the effects of spacer cation choice on the phase purity, and consequently optical properties, have been scarce.[36–39]

We have previously shown that high n = 2 phase purity films emitting pure blue emission could be obtained by the utilization of butylammonium (BA) instead of PEA.[21] This can be attributed to the strong interaction between PEA cations due to π–π stacking,[34] which favours the formation of the n = 1 phase.[19,21] Unfortunately, alkyl chain spacer cations result in perovskite films with inferior environmental stability[21] and lower light emission intensity compared to phenyl-ring containing spacers, such as PEA.[21,33] This can be attributed to the differences in crystal rigidity and electron–phonon coupling,[33] which are responsible for a significant difference in the photoluminescence quantum yield between PEA_2PbBr_4 and BA_2PbBr_4 (79% *vs.* 17%).[33] However, using mixed BA and PEA spacer cations allowed the formation of perovskite films combining the favourable properties of both BA and PEA to achieve brighter emission and improved environmental stability while maintaining phase purity.[21] Thus, here, we investigated the possibility of achieving phase purity *via* rational modifications of the spacer cation, instead of physical mixing of different cations. Knowing that the perovskites with phenyl ring-containing spacer cations typically exhibit bright emission but poor phase purity while alkyl chain-based spacer cations exhibit improved phase purity but less efficient emission,[19,21,33] we have conducted a systematic study that investigates the utilization of spacer cations containing both the aromatic ring and different alkylammonium moieties in order to gain an insight into the mechanisms governing the film properties. Therefore, thin films containing spacer cations with a phenyl ring and alkyl chains of different length, namely 1 carbon atom (benzylammonium, BZA), 2 carbon atoms (PEA), and 3 carbon atoms (phenylpropylammonium, PPA) have been prepared. The structure diagrams of the spacer cations are shown in Fig. S1, ESI.† These spacer cations have been previously investigated for solar cell applications, and while the length of the alkyl chain was found to affect the conductivity and photovoltaic performance, the effects on phase purity for low n numbers and LED performance were not investigated.

Our work demonstrates that the proportion of the n = 1 impurity phase decreases as the length of the aliphatic chain of the spacer cation increases and this trend holds for both methylammonium (MA) and formamidinium (FA) containing films. Consequently, we achieved high phase purity n = 2 films containing PPA cations and obtained sky blue emitting LEDs with the emission peak centered at ∼480 nm with the best maximum external quantum efficiency (EQE) of 3.35%. The reasons for the superior performance of PPA spacer cations are discussed in the following.

Results and discussion

Fig. 1 shows the absorption and PL spectra of MA- and FA-based perovskite films prepared with BZA, PEA, and PPA spacer cations corresponding to the stoichiometry of n = 2. As expected, based on common observations for quasi-2D RP perovskites, due to the energy funneling phenomenon, PL spectra can contain red-shifted peaks compared to the absorption spectra, indicating the presence of higher n phases at low enough content so that their presence is not necessarily observable in the absorption spectra and/or XRD patterns.[25,26] The peaks in the absorption and PL spectra for RP materials are located at similar positions for different spacer cations,[19,25–27] while the peak shape can indicate the presence of multiple n phases, *i.e.* a larger linewidth and symmetric lineshape are typically observed when contributions from different individual n phases could not be resolved. In contrast, single-phase samples, such as single crystals and exfoliated flakes, typically exhibit narrow asymmetric photoluminescence, with the exfoliated samples exhibiting more narrow emission with a lower emission tail due to their improved crystal quality and reduced defects.[27] In the MA series, we can clearly resolve absorption peaks corresponding to n = 1 (∼400 nm) and n = 2 (∼430 nm) for $BZA_2MAPb_2Br_7$, while the emission is located at ∼480 nm (likely corresponding to n = 4), with a small shoulder corresponding to n = 2 emission. In the case of $PEA_2MAPb_2Br_7$, the contribution of the n = 1 phase in the absorption spectrum diminishes, but there is a shoulder corresponding to the n = 3 phase at ∼450 nm. In the emission spectra, a single broad peak centered at ∼487 nm is observed, which likely corresponds to n = 4 with possible contributions of an n = 5 phase. Unlike the cases of BZA and PEA, where n = 1 absorption peaks are clearly present, in the absorption spectra of $PPA_2MAPb_2Br_7$, we can only resolve the peak corresponding to n = 2. A single emission peak is centered at ∼466 nm and likely corresponds to a small amount of the n = 3 phase that is not detectable in the absorption spectra. This phenomenon can be commonly observed in quasi-2D perovskites. For example, $PEA_2(Rb_{0.6}Cs_{0.4})_{n-1}Pb_nBr_{3n+1}$

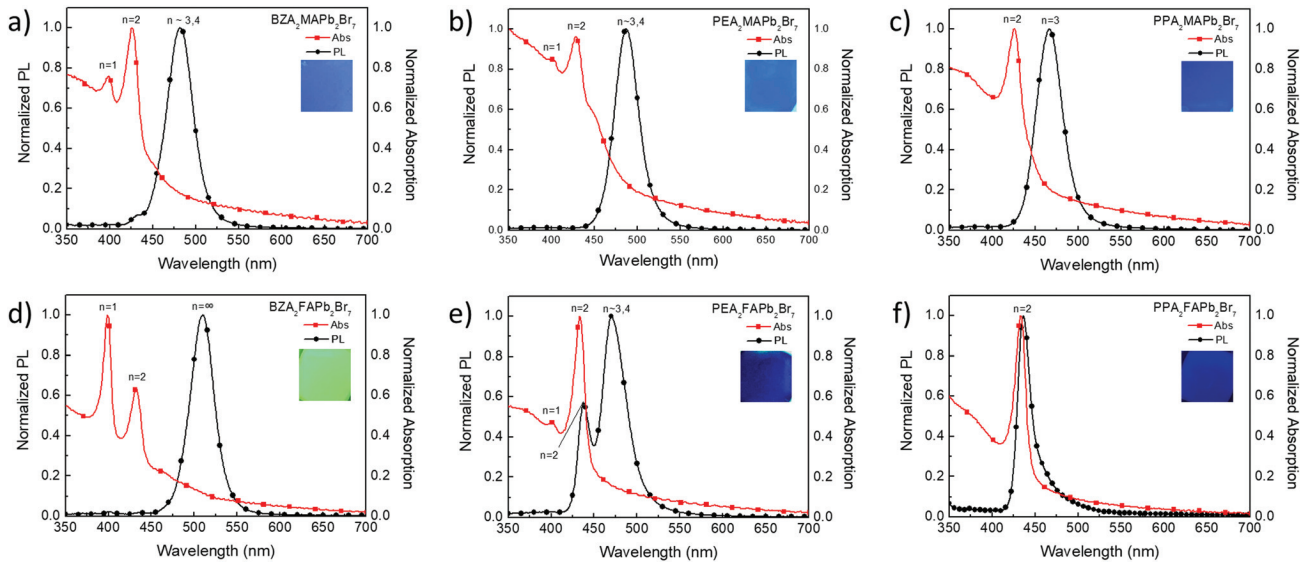

Fig. 1 Absorption and PL spectra of (a) $BZA_2MAPb_2Br_7$, (b) $PEA_2MAPb_2Br_7$, (c) $PPA_2MAPb_2Br_7$, (d) $BZA_2FAPb_2Br_7$, (e) $PEA_2FAPb_2Br_7$ and (f) $PPA_2FAPb_2Br_7$. The insets show the corresponding photos of the films under UV illumination.

samples with n = 2 stoichiometry exhibited PL from the n = 3 phase only, while the absorption spectrum was dominated by the n = 2 phase peak.[23] The presence of multiple phases in quasi-2D perovskites and the existence of energy funneling commonly result in a significant redshift of the emission peaks due to emission occurring from a small fraction of higher n phase. This shift is larger than the Stokes' shift corresponding to the difference in peak position of the absorption and emission peak corresponding to the same phase that can be observed in samples that do not contain higher n phases, such as quantum dots, and rarely thin films, for example, $PPA_2FAPB_2Br_7$ (Fig. 1f) and $BA_2MAPB_2Br_7$.[21] Some reported examples of the red-shift of emission in different RP perovskites due to energy funneling to higher n phases are summarized in Table S1, ESI.† Thus, the fact that the observed emission peak corresponds to the highest n phase with negligible contributions of lower n phases that are clearly observable in the absorption spectra indicates that the funneling process in MA-based films is very efficient.

In the FA series, we can also observe similar trends in terms of the diminishing proportion of the n = 1 phase as the length of the alkyl chain in the spacer cation increases. However, in this case, funneling is not as efficient as in the MA series, as evidenced by the presence of PL emission peaks corresponding to lower n phases indicating incomplete energy transfer from lower n to higher n phases in the samples exhibiting multiple phases in the absorption spectra. We observed multiple peaks in the emissions of $BZA_2FAPb_2Br_7$ and $PEA_2FAPb_2Br_7$, while for $PPA_2FAPb_2Br_7$, a single emission peak at ~436 nm is observed, which corresponds to n = 2, in agreement with the observed absorption spectrum. The shape of the emission peak resembles that observed for single-phase exfoliated flakes,[27] consistent with the high phase purity of the n = 2 sample. Since the choice of the small cation can affect the crystallization of the samples and thus the distribution of different phases, this likely contributes to the significant differences in funneling observed for the MA and FA series, since funneling is dependent on the average distance between low n and high n domains,[18] as well as the prevalence of higher n domains.[15,18] The distance between domains and the concentration of higher n domains are dependent on the film compositional distribution,[18] while the effects of distance and the dynamics of the process are dependent on the excited species (excitons *vs.* free carriers).[35]

Introducing various modifications of spacer cations has been explored in order to tune the phase distribution. It has been reported that a change in intermolecular interactions, such as hydrogen bonding, van der Waals interaction, aryl-perfluoroaryl and CH···π interactions between organic cations, affects the phase distribution, surface morphology and crystal orientation.[19,36,38] Also, it has been shown that even a small change in the structure of spacer cations, such as monofluorination, affects the packing arrangements of the organic cations and their orientational disorder.[39] In addition to the above mentioned modifications, the absorption spectra of both MA- and FA-based perovskites (Fig. 1) suggest that the length of the alkyl chain in the spacer cations also plays a significant role in the stabilization of the targeted n = 2 phase. In particular, as the length of the alkyl chain increases (from one carbon atom in the case of BZA to three carbon atoms in the case of PPA), the electron withdrawing effect of the nitrogen atom from the aromatic ring becomes less and less efficient. This, in turn, might allow for the observed stabilization of the n = 2 phase in the case of PPA due to the formation of stronger interactions between perovskite layers and organic bilayers compared to the shorter BZA and PEA cations.

Perovskite films with BZA, PEA and PPA cations have also been investigated *via* powder X-ray diffraction (PXRD). As can be seen from Fig. 2, the increase in the spacer cation length is

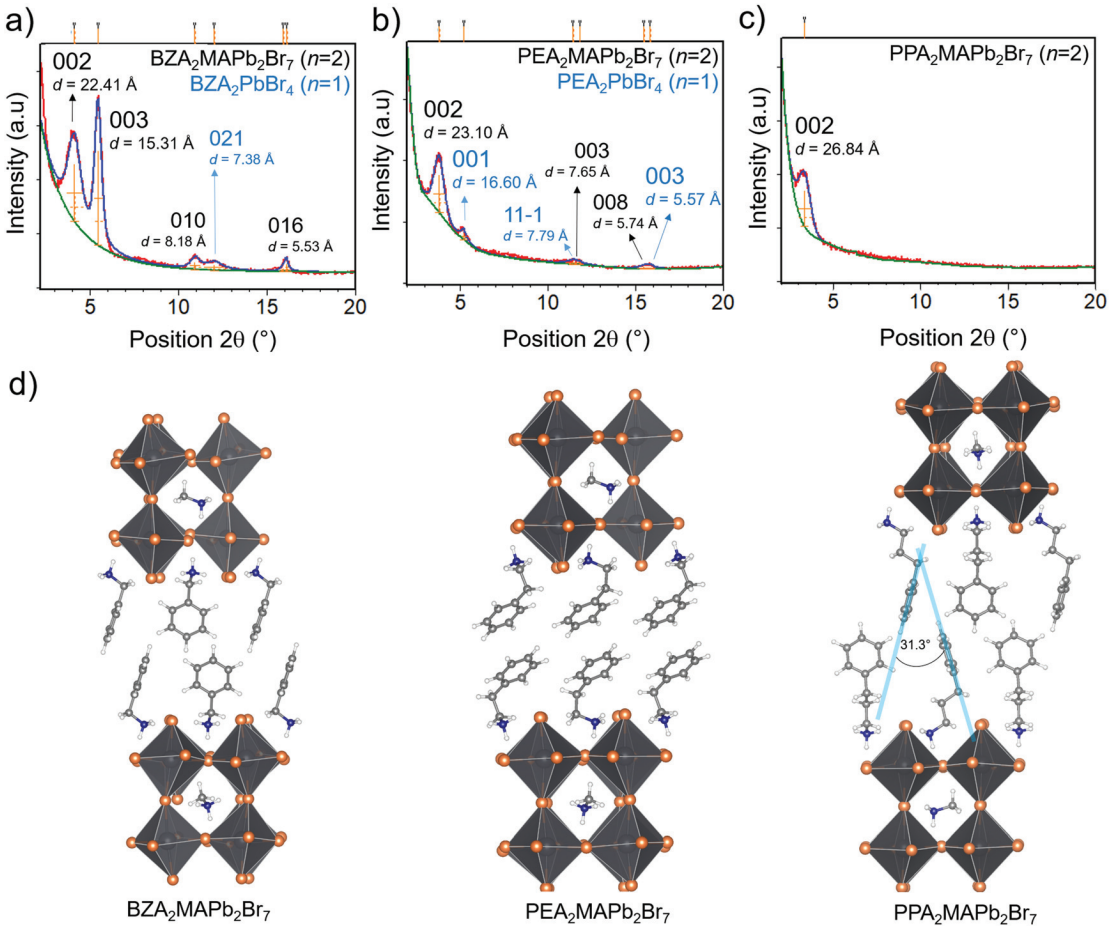

Fig. 2 Le Bail structural refinement on the XRD data of (a) $BZA_2MAPb_2Br_7$, (b) $PEA_2MAPb_2Br_7$, and (c) $PPA_2MAPb_2Br_7$. Panel (d) shows the perovskite structures with BZA, PEA and PPA cations, respectively.

accompanied with a shift of the 00*l* reflection towards lower 2θ angles, indicating an increment of bilayer thickness. A trend similar to that of the MA series has also been observed in the case of FA-based films (Fig. S2, ESI†), as expected. Since $n = 2$ structures of RP perovskites with BZA and PPA spacer cations have not been experimentally determined and reported so far, a synergic approach using PXRD structural analysis and computational calculations utilizing DFT has been undertaken in order to gain an insight into the structural features and packing arrangements for each spacer cation. Our previous work showed that the minimum energy structure of $PEA_2MAPb_2Br_7$ consists of off-centered parallel PEA cations within the spacer bilayer.[21] Fig. 2b shows the Le Bail refinement for $PEA_2MAPb_2Br_7$ converged with the refined cell of $a = 8.31(7)$ Å, $b = 8.12(5)$ Å, $c = 46.11(5)$ Å, $\alpha = 89.74(1)^\circ$, $\beta = 94.74(2)^\circ$ and $\gamma = 90.26(1)^\circ$. In addition to the reflections belonging to $n = 2$, XRD patterns also show diffraction lines that belong to the $n = 1$ PEA_2PbBr_4 phase. For the Le Bail refinement, the iodide analogue PEA_2PbI_4 lattice[40] has been used. The refinement for PEA_2PbBr_4 converged with $c = 17.41(2)$ Å, which is slightly smaller compared to the iodine analogue of 17.69 Å, as expected due to the smaller radius of Br^-.

In the course of structural relaxation calculation for the case of $BZA_2MAPb_2Br_7$, as a starting model, we have considered both the arrangement as reported for $n = 1$ BZA_2PbI_4[41] and the parallel offset stacking arrangement similar to one reported for PEA.[42] The difference between these models relates to the way phenyl moieties are mutually assembled within one layer. In the structure of BZA_2PbI_4, phenyl rings of BZA cations are assembled in a T-shaped fashion, while in the second model, rings within each layer were mutually parallel. The structural relaxation of the latter model yielded a minimum energy structure. The minimum energy structure, as derived from DFT calculations, has been used in the Le Bail refinement of PXRD data (Fig. 2a); the good agreement suggests that $BZA_2MAPb_2Br_7$ crystallizes with refined lattice parameters $a = 7.92(6)$ Å, $b = 8.18(4)$ Å, $c = 47.20(1)$ Å, $\alpha = 90.01(1)^\circ$, $\beta = 107.00(1)^\circ$ and $\gamma = 90.14(1)^\circ$. Again, as in the case of PEA-based films, diffraction lines that belong to the $n = 1$ BZA_2PbBr_4 can be observed in the PXRD pattern. The $n = 1$ structure exhibits the longest cell periodicity of 27.2(1) that is smaller, as anticipated, compared to its iodine analogue BZA_2PbI_4 reported by Papavassiliou *et al.*[41]

The minimum energy structures for $n = 2$ BZA and PEA-based perovskites are shown in Fig. 2d and it is essential to notice that the bilayer in both structures is characterized by a parallel assembly (orientation) of phenyl rings. Interestingly, in

the case of $PPA_2MAPb_2Br_7$, computational relaxation favours a quite different assembly of PPA cations compared to the shorter BZA and PEA cations, with the non-parallel arrangement of aromatic rings corresponding to the minimum energy structure. The angle between planes in which phenyl rings lay amounts to 31.3°. The lattice-parameters (a = 8.177 Å, b = 8.173 Å, c = 54.378 Å, α = 89.72°, β = 90.41° and γ = 90.18) obtained from the computational relaxation are in good agreement with the diffraction reflection of 002 at d = 26.84 Å. The observed change in the way aromatic rings are arranged in the structure of PPA compared to BZA and PEA is caused by the different interplay of intermolecular interactions, and is likely to have a significant impact on the phase distribution.[19,34,36] The parallel arrangement of the aromatic rings for BZA and PEA is a result of strong van der Waals interactions that consequently favor the formation of the n = 1 phase.[19] In contrast, the non-parallel arrangement of aromatic rings for PPA corresponds to weaker π–π interaction and enhanced CH···π interactions,[36] which could suppress the formation of the n = 1 phase. Structural features of minimum energy structures for n = 2 BZA, PEA and PPA-based perovskites, as obtained by the computational relaxation, are given in Table S2, ESI.†

Consequently, due to the enhanced phase purity and prominent blue emission, PPA-based perovskites are of interest for applications in blue LEDs. Since our target is to obtain emission in the blue spectral range, we will focus on the samples prepared with n = 2 solution stoichiometry. For samples prepared with n = 3, the presence of higher n phases results in a red shift of the emission, as shown in Fig. S3, ESI.† While the phase composition can be tuned to some degree under deposition conditions, for $n > 2$ solution stoichiometry, there is a significant emission contribution in the green spectral range. The device architecture and the SEM image of the cross-section are shown in Fig. S4, ESI.† SEM images and XRD patterns of $PPA_2MAPb_2Br_7$ and $PPA_2FAPb_2Br_7$ films are shown in Fig. S5 and S6, ESI,† respectively. From the SEM images, it can be observed that the film morphology is better for the MA-based films (fewer pinholes), but XRD patterns point to higher crystallinity in the case of the FA-based films. The higher crystallinity of FA-based films on indium tin oxide (ITO)/NiO_x/PVK is in agreement with the trends previously observed on ITO substrates (Fig. 2c and Fig. S2, ESI†). Since MA-based films exhibited better morphology while FA-based films exhibited crystallinity, we proceeded with the device fabrication for both types of small organic cations.

Fig. 3 shows the L–I–V curves of the $PPA_2MAPb_2Br_7$ champion device and EL spectra as a function of bias voltage. The results of a stability test of encapsulated devices in an ambient atmosphere at a constant bias voltage of 4 V are shown in Fig. S7, ESI† and a T_{50} value of ∼52 s was obtained. The devices exhibit sky-blue emission. While small spectral shifts can be observed, all the peak centers are within the 481 ± 3 nm spectral range and thus within the sky-blue spectral range. Furthermore, with increasing bias voltage, we observed a small blue shift in the emission peak, which is significantly different from the commonly observed red shift with increasing bias or

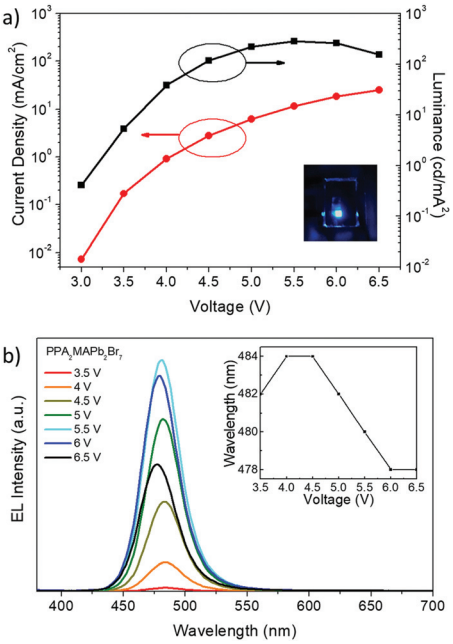

Fig. 3 (a) L–I–V plots (the device photo is shown in the inset) and (b) EL spectra *vs.* bias voltage for $PPA_2MAPb_2Br_7$ devices. The center wavelength position as a function of bias voltage is shown in the inset.

increasing operating time that has been attributed to Ostwald ripening or increases in grain/particle size,[23,24] as well as electrostatic effects and ion migration (the latter is applicable to mixed halide devices).[24] To establish whether bias resulted in any lasting changes in the sample composition, we measured the PL spectra in the device area and outside the device area for different bias voltages, as shown in Fig. S8, ESI.† We can observe that increasing bias results in a small blue shift of the PL, confirming that there is a permanent change in the film properties with increasing bias. The change can likely be attributed to small changes in sample crystal structure, *i.e.* contributions of different n phases to the emission. Changes in crystallinity could occur due to recrystallization due to Joule heating during bias treatment.[23] Since the peak shift is very small, any phase composition changes are too small to be detectable by other techniques, such as XRD, since PL is typically most sensitive to changes in the phase composition of the film. A small red shift of ∼2 nm in the EL emission at low bias likely originates from electrostatic effects,[24] consistent with the small magnitude of the peak shift and the fact that it does not appear in the PL spectra after bias, which only show a blue shift. The EL spectra are red-shifted compared to the PL spectra, similar to other reports on quasi-2D perovskite LEDs,[19,26,30–32] although in some cases no shifts were observed.[23,31] Such a red-shift is typically an indication of emission from a higher n phase,[19] while the differences reported in the literature could occur due to the differences in the sample composition, as well as differences in the mechanisms responsible for the funneling (Förster-type exciton transfer, as well as free-carrier charge transfer),[35] which can result in differences in the overall effect of the electric field on the peak position. In general,

excited species in PL are excitons (for low n phases that have a high exciton binding energy), while in EL, electrons and holes are injected from the opposite electrodes and they recombine in the active layer. In PL, carrier transfer between different phases occurs due to energy level differences at interfaces, while in EL, injected carriers are subjected to the external electric field that can enhance the funneling process and result in the majority of charges recombining in the smallest bandgap phase and consequently a red shift of the emission if there are higher n phases present.[26] In addition, differences in the excitation process between EL and PL can result in different carrier densities, which in turn would affect the light emission.[26]

Fig. 4 shows the EQE dependence on the bias, and illustrates the device reproducibility. The obtained devices exhibit an average EQE of 2.54 ± 0.45% (26 devices). The best performing device exhibits a maximum EQE of 3.35% and a maximum luminance of 286 cd m^{-2} (peak centered at 480 nm). This is significantly higher than that obtained for $PPA_2FAPb_2Br_7$ devices, which exhibit an average EQE of 0.07 ± 0.01% (7 devices), with the corresponding EL spectra and EQE histogram shown in Fig. S9, ESI.† The observed LED performance difference for MA- and FA-based perovskites is in agreement with the significantly higher photoluminescence quantum yield (PLQY) of 2.1% determined for $PPA_2MAPb_2Br_7$ films with trioctylphosphine oxide (TOPO)[26] as a passivating agent, compared to 0.16% obtained for $PPA_2FAPb_2Br_7$ films with TOPO. The differences between PLQY and EQE values are likely due to the fact that EQE is measured on a multilayered structure, which affects light extraction, and the fact that the substrate on which the perovskite film is deposited affects its quality.[17] Due to the fact that the perovskite LED structure contains multiple layers that emit light under optical excitation (PVK, TPBi), it is not possible to directly measure the PLQY of the perovskite film contained within the device. Furthermore, some differences in measured PLQY and EQE values can occur due to differences in achieved charge carrier densities in the emitting layer by optical excitation and electrical injection.

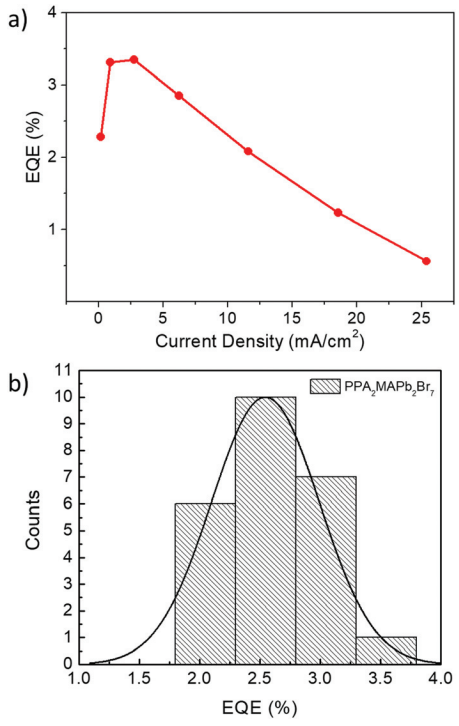

Fig. 4 (a) EQE *vs.* current density and (b) histogram plot illustrating the reproducibility of the $PPA_2MAPb_2Br_7$ devices (a total of 26 devices).

The obtained efficiency is significantly higher than that reported for PPA–Cs perovskite, where, in all cases, for different PPA : Cs ratios, green emission was obtained and the highest efficiency achieved was 0.01%.[12] It should also be noted that FA-based devices exhibit multiple emission peaks, consistent with the emission corresponding to the n = 2 phase and a large n or possibly 3D phase, while in MA-based devices, we observed emission corresponding to the n = 3 phase, as illustrated in Fig. S10, ESI.† The change in the optical properties for FA-based films compared to those deposited on ITO likely occurred due to differences in crystallization of the films on NiO_x/PVK, since the film quality of the perovskite is strongly dependent on the underlying material.[17] While the presence of additional phases is too small to be detectable from the comparison of XRD patterns of films on ITO and ITO/NiO_x/PVK (Fig. 2c and Fig. S2, Fig. S6, ESI†), the presence of different n phases is very clear in the absorption and PL spectra. From the obtained absorption and PL spectra shown in Fig. S10, ESI,† we can conclude that in MA-based films, efficient funneling occurs from the dominant n = 2 phase to the small amount of n = 3 and 4 phases, leading to efficient sky-blue device performance. In contrast, there is no efficient funneling from the n = 2 phase to a green emitting higher n/3D phase in the FA-based films, resulting in multiple emission peaks and low efficiency. It is known that a non-optimized energy landscape, which lacks a suitable distribution of different bandgap energy domains that can facilitate energy transfer, leads to significantly lower emission efficiency.[15] Since funneling is dependent not only on the concentrations of phases with higher n but also on the distance between them,[18] the increased crystallinity of FA-based films could result in increased distances between the lower n and higher n phases and consequently incomplete energy transfer.

Thus, the probable reason for the inferior performance of FA-based devices is the non-optimized compositional n number distribution, preventing efficient energy transfer from the dominant wide bandgap n = 2 phase to a small amount of high n or 3D impurity phase (which cannot be resolved using XRD, but could explain the small tail in the luminescence). In both the absorption spectra and XRD patterns, only the n = 2 phase can be resolved, while in the PL spectra, we can observe the peaks corresponding to n = 2, n = 3, and a higher n ($\geq$8) phase, showing a clear lack of intermediate phases between n = 3 and higher n, which would impede efficient energy transfer to the high n phase. Thus, despite the lower crystallinity, $PPA_2MAPb_2Br_7$ emitters exhibit superior performance in sky-blue LEDs, facilitated by favourable energy funneling from the dominant n = 2 phase to n = 3, 4 phases contributing to sky-blue emission. In contrast, devices with $BZA_2MAPb_2Br_7$ and

$PEA_2MAPb_2Br_7$ emitters exhibit green light emission, with the emission center located above 500 nm, as shown in Fig. S11, ESI.†

Experimental section

Materials

Phenylpropylammonium bromide (PPABr) and formamidinium bromide (FABr) were purchased from Xi'an Polymer Light Technology Corp. Benzylammonium bromide (BZABr), phenethylammonium bromide (PEABr), and methylammonium bromide (MABr) were purchased from Greatcell Solar Materials. Lead bromide ($PbBr_2$, 99.998%), acetonitrile (ACN, anhydrous, 99.8+%), isopropanol (IPA, anhydrous, 99.5+%), *N*,*N*-dimethylformamide (DMF, anhydrous, 99.9%) and trioctylphosphine oxide (TOPO, 98%) were obtained from Alfa Aesar. Nickel(II) acetate tetrahydrate ($Ni(Ac)_2{\cdot}4H_2O$, 99.998%), chlorobenzene (anhydrous, 99.8%), methyl acetate (MAc, anhydrous, 99.5%), and ethanolamine ($\geq$99%) were purchased from Sigma Aldrich. Poly(9-vinylcarbazole) (PVK), 1,3,5-tris(1-phenyl-1*H*-benzimidazol-2-yl)benzene (TPBi, >99.5%) and cesium carbonate (Cs_2CO_3, >99.994%) were purchased from Luminescence Technology Corp. Hexafluorotetracyanonaphthoquinodimethane (F6TCNNQ, 99%) was purchased from Shanghai Da Ran Chemicals. Aluminum pellets (Al, 99.999%) were purchased from Kurt J. Lesker Company. All chemicals were used as received unless otherwise specified.

Synthesis of quasi-2D perovskite thin films

The perovskite precursor solution was prepared by dissolving the mixture of precursors according to the corresponding stoichiometric ratio in DMF. For instance, the precursor solution of $PPA_2MAPb_2Br_7$ was obtained by dissolving $PbBr_2$ (0.1 mmol, 36.7 mg), PPABr (0.1 mmol, 21.6 mg) and MABr (0.05 mmol, 5.6 mg) in 1 mL of DMF, followed by stirring at room temperature. Perovskite films were then deposited on cleaned ITO glass substrates by spin-coating at 1000 rpm for 10 s and then 4000 rpm for 45 s. 50 μL of MAc antisolvent was added to the film after 5 s of spinning at 4000 rpm. The film was then vacuum dried for 30 min before any further treatment or characterization. All procedures were performed inside an argon filled glovebox.

Characterization of quasi-2D perovskite films

All optical measurements were performed with perovskite films encapsulated by quartz plates. Steady state PL spectra were recorded using a PDA-512 USB (Control Development Inc.) The fiberoptic spectrometer used a He–Cd laser (325 nm) as the excitation source. Absorption spectra of the perovskite films were recorded using a Cary 50 UV-Vis spectrometer (Agilent Technologies). XRD patterns of the perovskite samples were obtained using a Rigaku SmartLab 9 kW X-ray Diffractometer with Cu Kα radiation. A Hitachi S-4800FEG Scanning Electron Microscope was used for morphology characterization of the perovskite films. External PLQY was estimated through a comparison technique of the encapsulated perovskite films with the standard reference. PL of perovskite samples and the standard reference was recorded using the same setup under the same conditions. A He–Cd 325 nm continuous wave laser was used as the excitation source. The absorption of the samples was determined by the evaluation of incident power, reflected power, and transmitted power of the laser, which were measured by a calibrated photodiode power meter from Newport. The PLQY of the perovskite films was then calculated by comparing their PL intensity and absorption intensity ratio with those of the standard reference, as described previously.[21]

Device fabrication and characterization

The LED structure was ITO/NiO_x/F6TCNNQ/PVK/perovskite/TPBi/Cs_2CO_3/Al. Patterned ITO/glass substrates were cleaned sequentially using Decon 90, deionized water, acetone and ethanol, followed by oxygen plasma cleaning before use. NiO_x sol–gel solution was prepared by dissolving $Ni(Ac)_2{\cdot}4H_2O$ (0.2 mmol) and ethanolamine (0.2 mmol) in 1 mL of IPA and stirring overnight at 70 °C. The NiO_x sol–gel solution was spin-coated on ITO/glass substrates at 3000 rpm for 30 s followed by preheat treatment at 100 °C for 10 min and later annealing at 275 °C for 1 h in air. The F6TCNNQ solution (0.2 mg mL^{-1} in ACN) was then spin-coated on NiO_x at 4000 rpm for 60 s inside an argon-filled glovebox. NiO_x/F6TCNNQ films were annealed overnight at 80 °C. PVK solution (5 mg mL^{-1} in CB) was spin-coated on NiO_x/F6TCNNQ at 3000 rpm for 30 s followed by annealing at 120 °C for 15 min. Perovskite films were then deposited on the NiO_x/F6TCNNQ/PVK layer as described above. TOPO solution (0.5 mg mL^{-1} in MAc) was further spin-coated on the perovskite layer for surface passivation. Finally, TPBi, Cs_2CO_3 and Al were sequentially thermally evaporated through a shadow mask with the thickness of 45 nm, 1 nm, and 100 nm, respectively, to complete the device. The active area defined by the mask was 0.04 cm^2. The performance of the perovskite LEDs was characterized by an electroluminescence (EL) measuring setup consisting of a programmable Keithley 2400 SourceMeter and a Photoresearch PR-670 spectroradiometer with SL-1X close-up lens. EL spectra were recorded using a PR670 spectroradiometer.

DFT calculations

Density functional theory (DFT) calculations have been performed using the mixed Gaussian and plane-wave basis code CP2K[43] with the GTH-PBE pseudopotentials[44–46] and PBE + D3[47,48] exchange–correlation functional. Valence electrons were described by triple-zeta plus two polarizations Gaussian basis set.[49] The first Brillouin zone was sampled by the Monkhorst–Pack *k*-point mesh with the density of 5 Å. The unit cell and the atoms were relaxed until the maximal force on any atom was smaller than 0.02 eV $Å^{-1}$, and the pressure was smaller than 0.01 GPa.

Conclusion

This work investigated the opportunity to tune the opto-electronic properties of quasi-2D perovskites through careful

compositional engineering and demonstrated that the length of the alkylammonium tail of alkyl-phenyl-based spacer cations consisting of a phenyl ring and an alkyl chain influenced the arrangement of the spacer cations, which in turn significantly affected the phase distribution in the prepared films. The utilization of shorter alkyl chains with 1 and 2 carbon atoms resulted in the parallel assembly of phenyl rings within the organic bilayer, which favored the formation of the $n = 1$ phase. Consequently, due to a change in solution stoichiometry, the appearance of the $n = 1$ phase also additionally led to the formation of higher n phases, which resulted in an undesirable shift of emission wavelength into the green spectral region. On the other hand, when longer 3-carbon chains are introduced, a non-parallel assembly of phenyl rings arises that proves to be beneficial for suppression of the $n = 1$ phase. As a result of such an approach, films that exhibit blue emission are readily obtained, and sky blue LEDs with an efficiency of 3.35% are demonstrated. Thus, our work explains how the structural characteristics of the spacer cation affect the crystallization and phase composition of perovskite films, which can facilitate the design of spacer cations for efficient bromide-only blue emitting perovskite materials.

Conflicts of interest

There are no conflicts to declare.

Acknowledgements

This work was supported by the Seed Funding for Basic Research and Seed Funding for Strategic Interdisciplinary Research Scheme of the University of Hong Kong and Project PZS-2019-02-2068 financed by the ''Research Cooperability'' Program of the Croatian Science Foundation funded by the European Union from the European Social Fund under the Operational Programme Efficient Human Resources 2014–2020. The authors also acknowledge the financial support from Shenzhen Science and Technology Commission Projects JCYJ20160530184523244 and JCYJ20170818141216288, the European Union through the European Regional Development Fund – the Competitiveness and Cohesion Operational Programme (KK.01.1.1.06), and the Croatian–Chinese bilateral project entitled ''Quasi 2D organic–inorganic perovskites for light emitting applications''.

Notes and references

1 M. Lu, Y. Zhang, S. Wang, J. Guo, W. W. Yu and A. L. Rogach, *Adv. Funct. Mater.*, 2019, **29**, 1902008.
2 N. K. Kumawat, X. K. Liu, D. Kabra and F. Gao, *Nanoscale*, 2019, **11**, 2109.
3 C. H. A. Li, Z. Zhou, P. Vashishtha and J. E. Halpert, *Chem. Mater.*, 2019, **31**, 6003.
4 Z. Chen, Y. Guo, E. Wertz and J. Shi, *Adv. Mater.*, 2019, **31**, 1803514.
5 X. Gao, X. Zhang, W. Yin, H. Wang, Y. Hu, Q. Zhang, Z. Shi, V. L. Colvin, W. W. Yu and Y. Zhang, *Adv. Sci.*, 2019, **20**, 1900941.
6 H. D. Lee, H. Kim, H. Cho, W. Cha, Y. Hong, Y. H. Kim, A. Sadhanala, V. Venugopalan, J. S. Kim, J. W. Choi, C. L. Lee, D. Kim, H. Yang, R. H. Friend and T. W. Lee, *Adv. Funct. Mater.*, 2019, **29**, 1901225.
7 J. Qing, C. Kuang, H. Wang, Y. Wang, X. K. Liu, S. Bai, M. Li, T. C. Sum, Z. Hu, W. Zhang and F. Gao, *Adv. Mater.*, 2019, **31**, 1904243.
8 Y. Han, S. Park, C. Kim, M. Lee and I. Hwang, *Nanoscale*, 2019, **11**, 3546.
9 P. Vashishtha, M. Ng, S. B. Shivarudraiah and J. E. Halpert, *Chem. Mater.*, 2019, **31**, 83.
10 B. Zhao, S. Bai, V. Kim, R. Lamboll, R. Shivanna, F. Auras, J. M. Richter, L. Yang, L. Dai, M. Alsari, X. J. She, L. Liang, J. Zhang, S. Lilliu, P. Gao, H. J. Snaith, J. Wang, N. C. Greenham, R. H. Friend and D. Di, *Nat. Photonics*, 2018, **12**, 783.
11 R. Yang, R. Li, Y. Cao, Y. Wei, Y. Miao, W. L. Tan, X. Jiao, H. Chen, L. Zhang, Q. Chen, H. Zhang, W. Zou, Y. Wang, M. Yang, C. Yi, N. Wang, F. Gao, C. R. McNeill, T. Qin, J. Wang and W. Huang, *Adv. Mater.*, 2018, **30**, 1804771.
12 X. Xu, Z. Wang, J. Yu, L. Li and X. Yan, *Nanoscale Res. Lett.*, 2019, **14**, 255.
13 J. Yan, G. Croes, A. Fakharuddin, W. Song, P. Heremans, H. Chen and W. Qui, *Adv. Opt. Mater.*, 2019, **7**, 1900465.
14 H. Tsai, W. Nie, J. C. Blancon, C. C. Stoumpos, C. M. M. Soe, J. Yoo, J. Crochet, S. Tretiak, J. Even, A. Sadhanala, G. Azzellino, R. Brenes, P. M. Ajayan, V. Bulović, S. D. Stranks, R. H. Friend, M. G. Kanatzidis and A. D. Mohite, *Adv. Mater.*, 2018, **30**, 1704217.
15 L. N. Quan, Y. Zhao, F. P. G. de Arquer, R. Sabatini, G. Walters, O. Voznyy, R. Comin, Y. Li, J. Z. Fan, H. Tan, J. Pan, M. Yuan, O. M. Bakr, Z. Lu, D. H. Kim and E. H. Sargent, *Nano Lett.*, 2017, **17**, 3701.
16 Y. Zou, H. Xu, S. Li, T. Song, L. Kuai, S. Bai, F. Gao and B. Sun, *ACS Photonics*, 2019, **6**, 1728.
17 Z. Ren, X. Xiao, R. Ma, H. Lin, K. Wang, X. W. Sun and W. C. H. Choy, *Adv. Funct. Mater.*, 2019, **29**, 1905339.
18 N. Yantara, A. Bruno, A. Iqbal, N. F. Jamaludin, C. Soci, S. Mhaisalkar and N. Mathews, *Adv. Mater.*, 2018, **30**, 1800818.
19 J. Xing, Y. Zhao, M. Askerka, L. N. Quan, X. Gong, W. Zhao, J. Zhao, H. Tan, G. Long, L. Gao, Z. Yang, O. Voznyy, J. Tang, Z. H. Lu, Q. Xiong and E. H. Sargent, *Nat. Commun.*, 2018, **9**, 3541.
20 Y. Hu, L. M. Spies, D. Alonso-Álvarez, P. Mocherla, H. Jones, J. Hanisch, T. Bein, P. R. F. Barnes and P. Docampo, *J. Mater. Chem. A*, 2018, **6**, 22215.
21 T. L. Leung, H. W. Tam, F. Z. Liu, J. Y. Lin, A. M. C. Ng, W. K. Chan, W. Chen, Z. B. He, I. Lončarić, L. Grisanti, C. Ma, K. S. Wong, Y. S. Lau, F. R. Zhu, Ž. Skoko, J. Popović and A. B. Djurišić, *Adv. Opt. Mater.*, 2020, **8**, 1901679.
22 Z. C. Li, Z. M. Chen, Y. C. Yang, Q. F. Xue, H. L. Yip and Y. Cao, *Nat. Commun.*, 2019, **10**, 1027.
23 Y. Z. Jiang, C. C. Qin, M. H. Cui, K. K. Liu, Y. M. Huang, M. H. Luo, L. Zhang, H. Y. Xu and S. S. Li, *Nat. Commun.*, 2019, **10**, 1868.

24 P. Vashishtha and J. E. Halpert, *Chem. Mater.*, 2017, **29**, 5965.
25 D. N. Congreve, M. C. Weidman, M. Seitz, W. Paritmongkol, N. S. Dahod and W. A. Tisdale, *ACS Photonics*, 2017, **4**, 476.
26 X. L. Yang, X. W. Zhang, J. X. Deng, Z. Chu, Q. Jiang, J. H. Meng, P. Y. Wang, L. Q. Zhang, Z. G. Yin and J. B. You, *Nat. Commun.*, 2018, **9**, 570.
27 K. Leng, I. Abdelwahab, I. Verzhbitskiy, M. Telychko, L. Q. Chu, W. Fu, X. Chi, N. Guo, Z. H. Chen, Z. X. Chen, C. Zhang, Q. H. Xu, J. Lu, M. Chhowalla, G. Eda and K. P. Loh, *Nat. Mater.*, 2018, **208**(17), 908.
28 W. Deng, X. C. Jin, Y. Lv, X. J. Zhang, X. H. Zhang and J. S. Jie, *Adv. Funct. Mater.*, 2019, **29**, 1903861.
29 H. Lin, J. Mao, M. C. Qin, Z. L. Song, W. J. Yin, X. H. Lu and W. C. H. Choy, *Nanoscale*, 2019, **11**, 16907.
30 S. Zeng, S. Shi, S. Wang and Y. Xiao, *J. Mater. Chem. C*, 2020, **8**, 1319.
31 S. Kumar, J. Jagielski, S. Yakunin, P. Rice, Y. Chiu, M. Wang, G. Nedelcu, Y. Kim, S. Lin, E. J. G. Santos, M. V. Kovalenko and C. Shih, *ACS Nano*, 2016, **10**, 9720.
32 S. Lee, D. Kim, I. Hamilton, M. Daboczi, Y. S. Nam, B. R. Lee, B. Zhao, C. H. Jang, R. H. Friend, J. Kim and M. H. Song, *Adv. Sci.*, 2018, **5**, 1801350.
33 X. Gong, O. Voznyy, A. Jain, W. Liu, R. Sabatini, Z. Piontkowsky, G. Walters, G. Bappi, S. Nokhrin, O. Bushuyev, M. Yuan, R. Comin, D. McCamant, S. O. Kelley and E. H. Sargent, *Nat. Mater.*, 2018, **17**, 550.
34 M. Y. Ban, Y. T. Zou, J. P. H. Rivett, Y. G. Yang, T. H. Thomas, Y. S. Tan, T. Song, X. Y. Gao, D. Credgington, F. Deschler, H. Sirringhaus and B. Q. Sun, *Nat. Commun.*, 2018, **9**, 3892.
35 A. H. Proppe, M. H. Elkins, O. Voznyy, R. D. Pensack, F. Zapata, L. V. Besteiro, L. N. Quan, R. Quintero-Bermudez, P. Todorovic, S. O. Kelley, A. O. Govorov, S. K. Gray, I. Infante, E. H. Sergeant and G. D. Scholes, *J. Phys. Chem. Lett.*, 2019, **10**, 419.
36 L. Yan, J. Hu, N. Zhou, A. M. Moran and W. You, *Sol. RRL*, 2020, **4**, 1900374.
37 B. E. Cohen, M. Wierzbowska and L. Etgar, *Sustainable Energy Fuels*, 2017, **1**, 1935.
38 J. Hu, I. W. H. Oswald, H. Hu, S. J. Stuard, M. M. Nahid, L. Yan, Z. Chen, H. Ade, J. R. Neilson and W. You, *ACS Mater. Lett.*, 2019, **1**, 171.
39 J. Hu, I. W. H. Oswald, S. J. Stuard, M. M. Nahid, N. Zhou, O. F. Williams, Z. Guo, L. Yan, H. Hu, Z. Chen, X. Xiao, Y. Lin, Z. Yang, J. Huang, A. M. Moran, H. Ade, J. R. Neilson and W. You, *Nat. Commun.*, 2019, **10**, 1276.
40 J. Calabrese, N. L. Jones, R. L. Harlow, N. Herron, D. L. Thorn and Y. Wang, *J. Am. Chem. Soc.*, 1991, **113**, 2328.
41 G. C. Papavassiliou, G. A. Mousdis, C. P. Raptopoulou and A. Terzis, *Z. Naturforsch., B: J. Chem. Sci.*, 1999, **54**, 1405.
42 A. H. Slavney, R. W. Smaha, I. C. Smith, A. Jaffe, D. Umeyama and H. I. Karundasa, *Inorg. Chem.*, 2017, **56**, 46.
43 J. Hutter, M. Iannuzzi, F. Schiffmann and J. VandeVondele, *Wiley Interdiscip. Rev.: Comput. Mol. Sci.*, 2014, **4**, 15.
44 S. Goedecker, M. Teter and J. Hutter, *Phys. Rev. B: Condens. Matter Mater. Phys.*, 1996, **54**, 1703.
45 C. Hartwigsen, S. Goedecker and J. Hutter, *Phys. Rev. B: Condens. Matter Mater. Phys.*, 1998, **58**, 3641.
46 M. Krack, *Theor. Chem. Acc.*, 2005, **114**, 145.
47 S. Grimme, J. Antony, S. Ehrlich and S. Krieg, *J. Chem. Phys.*, 2010, **132**, 154104.
48 S. Grimme, S. Ehrlich and L. Goerigk, *J. Comput. Chem.*, 2011, **32**, 1456.
49 J. VandeVondele and J. Hutter, *J. Chem. Phys.*, 2007, **127**, 114105.